Journal of the European Ceramic Society 43 (2023) 1605–1612

Contents lists available at ScienceDirect

Journal of the European Ceramic Society

journal homepage: www.elsevier.com/locate/jeurceramsoc

Electrical performance of orthotropic and isotropic 3YTZP composites with graphene fillers

C. López-Pernía [a], C. Muñoz-Ferreiro [a], R. Moriche [a], A. Morales-Rodríguez [a], Á. Gallardo-López [a], R. Poyato [b,*]

[a] Depto. de Física de la Materia Condensada, ICMS, CSIC-Universidad de Sevilla, Apdo. 1065, Sevilla 41080, Spain
[b] Instituto de Ciencia de Materiales de Sevilla, ICMS, CSIC-Universidad de Sevilla, Avda. Américo Vespucio 49, Sevilla 41092, Spain

ARTICLE INFO

Keywords:
Graphene-based nanostructures (GBN)
Aspect ratio
Zirconia
Electrical conductivity
Percolation threshold

ABSTRACT

3 mol% yttria tetragonal zirconia polycrystal (3YTZP) composites with orthotropic or isotropic microstructures were obtained incorporating few layer graphene (FLG) or exfoliated graphene nanoplatelets (e-GNP) as fillers. Electrical conductivity was studied in a wide range of contents in two configurations: perpendicular ($\sigma_{\perp}$) and parallel ($\sigma_{//}$) to the pressing axis during spark plasma sintering (SPS). Isotropic e-GNP composites presented excellent electrical conductivity for high e-GNP contents ($\sigma_{\perp} \sim 3200$ S/m and $\sigma_{//} \sim 1900$ S/m for 20 vol% e-GNP), consequence of their misoriented distribution throughout the matrix. Optimum electrical performance was achieved in the highly anisotropic FLG composites, with high electrical conductivity for low contents ($\sigma_{\perp} \sim 680$ S/m for 5 vol%), percolation threshold below 2.5 vol% FLG and outstanding electrical conductivity for high contents ($\sigma_{\perp} \sim 4000$ S/m for 20 vol%), result of the high aspect ratio and low thickness of FLG.

1. Introduction

The research activity on ceramic composites with graphene-based nanomaterials (GBN) as fillers has remarkably increased in the last decade, with a highly noticeable rise in the number of published papers and patents since 2016 [1]. The interest in this topic is a consequence of the wide range of potential applications of these composites, which include energy production and storage, electromagnetic interference shields, thermal management or protection, structural engineering applications or use as biomaterial, among others [1–5].

Up to date, most of the studies on graphene/ceramic composites have reported fabrication of the composites by spark plasma sintering (SPS), as this technique allows the obtaining of highly densified materials in very short sintering times, avoiding degradation of the nanostructures under prolonged exposure to high temperatures. It is well known that the application of uniaxial pressure during SPS usually results in the preferential alignment of the graphene nanostructures perpendicularly to the pressing direction, as consequence of their 2D nature and high aspect ratio [6]. This microstructural design results in highly anisotropic electrical and thermal properties, with remarkably higher conductivities in the plane in which the GBN are preferentially oriented [7–11]. The anisotropy in electrical and thermal properties has been pointed out as highly suitable for some applications. Chen et al. [4] reported SiC composites with self-aligned graphene nanoplatelets (GNP) as promising high-performance electromagnetic interference (EMI) shielding materials. The texture distribution of the GNP was pointed out as the main reason for the high shielding effectiveness value of the SiC/GNP composites. Çelik et al. [12] highlighted that the higher in-plane thermal conductivity in Al_2O_3/GNP composites can be beneficial for applications that require dissipation of heat in one direction, increasing the efficiency of engineering processes where heat dissipation is demanded. Regarding mechanical properties, it has been reported [13,14] that the orthotropic composites can be markedly tougher and suitable especially in those structural applications under uniaxial loading where the cracks, once nucleated, propagate perpendicularly to the GNP.

In recent years, research in graphene/ceramic composites has extended to the study of isotropic composites that could respond to applications for which anisotropic composites are not suitable, as structural applications under multi-axial loading where cracks can propagate in any direction, or electro-discharge machining (EDM) in random directions to obtain pieces with complex geometries as required by industry. In order to achieve an isotropic microstructure in the composites several approaches have been addressed. Some authors avoided the application of pressure during sintering by using a

* Corresponding author.
E-mail address: rosalia.poyato@icmse.csic.es (R. Poyato).

https://doi.org/10.1016/j.jeurceramsoc.2022.11.068
Received 12 September 2022; Received in revised form 21 November 2022; Accepted 27 November 2022
Available online 28 November 2022

conventional furnace [15] or by means of pressureless ultrafast sintering [16] to elude the self-alignment of the nanostructures. In other studies, the size and thickness of the GBN were accurately reduced by high-energy milling [17,18] or adequate selection of solvent in a wet powder processing routine [13], and dense composites were subsequently fabricated by spark plasma sintering. Very recently, a few studies have reported the comparison of the different performance of both types of ceramic composites -orthotropic vs isotropic- in terms of their hydrothermal ageing resistance [19] or mechanical properties [13,14]. However, a detailed analysis and comparison of the different electrical performance of orthotropic/isotropic composites is still lacking.

In our previous studies, we have optimized the processing routines to prepare orthotropic and isotropic zirconia composites in a controlled way. The homogenization of the composite powder in a high-energy planetary ball mill in dry conditions has been shown to promote the exfoliation and fragmentation of the as-received GNP which, combined with SPS, allows the obtaining of highly dense composites with randomly oriented exfoliated GNP (e-GNP) despite the application of uniaxial pressure [17–19]. On the other hand, a low-energy powder processing by bath sonication that does not introduce significant changes on the GBN structure or dimensions has been shown to be a very convenient routine to obtain SPSed highly anisotropic zirconia composites with high aspect ratio few-layer graphene as filler [9,20].

In this work, the electrical conductivity of 3YTZP/GBN composites with tailored microstructures and GBN in a wide range of contents (1, 2.5, 5, 10 and 20 vol%) has been studied. Composites with orthotropic or isotropic microstructures have been obtained by incorporating few layer graphene (FLG) or exfoliated graphene nanoplatelets (e-GNP), respectively, as fillers, by spark plasma sintering (SPS) at two different sintering temperatures. The effects of the aspect ratio, number of graphene layers and presence of defects in the GBN structure on the electrical conductivity and percolation threshold of the two types of composites have been analyzed. Tailoring of the electrical performance of ceramic-graphene composites is a key factor in order to fulfill the requirements of the different engineering applications where these materials can be used.

2. Experimental procedure

Two different graphene-based nanomaterials (Angstrom Materials, Dayton, Ohio, USA) were used as fillers: (i) few layer graphene (FLG, lateral dimension $\leq$10 μm and $\leq$3 graphene layers, ref. N002-PDR-HD) and (ii) graphene nanoplatelets (GNP, lateral dimension <5 μm and 10–20 nm thickness, ref. N006-P). For the ceramic matrix, 3 mol% yttria tetragonal zirconia polycrystal powders with 40 nm particle size (3YTZP, ref. TZ-3YB-E, Tosoh Corporation, Tokyo, Japan) were used after an annealing treatment at 850 °C for 30 min in air.

Composite powders with 1, 2.5, 5, 10 and 20 vol% GBN were prepared by means of two different powder processing routines. For the composites hereinafter named as FLG composites, a suspension of the FLG in isopropyl alcohol was subjected to ultrasonic agitation for 30 min by means of an ultrasonic bath (Clifton™, Fischer Scientific S.L., Madrid, Spain). The 3YTZP powder was added to the FLG suspension and sonicated for 5 min. The composite powders were homogenized in an agate mortar after drying on a hot plate with continuous magnetic stirring. For the composites hereinafter named as e-GNP composites, the as-received GNP and the zirconia powder were planetary ball milled (Pulverisette 7, Fritsch classic line, Fritsch, Germany) under dry conditions at a speed of 350 rpm for 4 h. The milling media consisted of seven 15 mm diameter zirconia balls in a 45 mL zirconia vial. This processing route has been shown to promote a drastic reduction of the lateral size ($\leq$0.6 μm) and thickness (less than 10 graphene layers) of the as-received GNP, allowing the fabrication of composites with multilayer graphene as filler from cost-effective graphene nanoplatelets [17,18].

The composite powders were spark plasma sintered at 1250 and 1300 °C for 5 min, with an applied pressure of 75 MPa (SPS model 515 S, Dr. Sinter, Inc., Kanagawa, Japan, Centro de Investigación, Tecnología e Innovación de la Universidad de Sevilla, CITIUS) operating under vacuum. A sheet of graphite paper was placed between the powders and the die/punches to ensure their electrical, mechanical and thermal contact and also for easy removal. The temperature was monitored by means of an optical pyrometer focused on the side of the graphite die.

The semi-quantitative analysis of the crystallographic phases present in the sintered composites was carried out by X-Ray diffraction (XRD) at CITIUS in a D8 Advanced A25 X-Ray diffractometer (Bruker Co. Massachussetts, USA).

The density of the composites was measured with the Archimedes' method using distilled water as the immersion medium. The theoretical densities for the composites with different GBN contents were calculated by the rule of mixtures taking the density of the 3YTZP and the GBN as 6.05 g/cm^3 and 2.2 g/cm^3, respectively (data from the suppliers). The possible structural modifications of the GBN in the composites after the powders processing and sintering were assessed by Raman spectroscopy using a LabRam HR800 spectrometer (Horiba Jobin Yvon, Kyoto, Japan) operating with a 20 mW He-Ne green laser (Instituto de Ciencia de Materiales de Sevilla, ICMS). To that end, five to ten spectra were acquired on the as-received GNP and FLG, and on the fracture surfaces of the sintered composites. The GBN distribution in the zirconia matrix was inspected on cross-section (c.s.) surfaces polished up to 1 μm by low magnification conventional scanning electron microscopy (SEM, FEI-Teneo, FEI, USA, CITIUS) using backscattered electrons (BSE) for imaging.

The DC electrical conductivity of the sintered composites was estimated at room temperature using the capacitive method. To that end, the samples were cut into parallelepipedic specimens, two parallel faces were coated with colloidal silver paste, and the electrodes were fired at 600 °C for 30 min under Ar flow to avoid air degradation of the GBN during the process. In order to account for any degree of electrical anisotropy, two different electrode configurations were used to obtain the electrical conductivity in the directions parallel ($\sigma_{//}$) and perpendicular ($\sigma_{\perp}$) to the compression axis during SPS (Fig. 1). The equipment used to evaluate the electrical conductivity was a Solartron SI1260A analyzer, which used a potentio-dynamic method with a 0–10 mV range in steps of 1 mV (CITIUS). The measurements were validated also in AC, with a frequency sweep from 100 to 1000 Hz at 10 mV. Several measurements were taken in each configuration. For each measurement, the electrodes were removed with acetone and new colloidal silver paste was applied and fired.

3. Results and discussion

3.1. Microstructural characterization

The XRD analysis conducted on the FLG and e-GNP composites indicated the presence of reduced tetragonal zirconia ($ZrO_{1.95}$) (PDF 81–1544, ICDD) as the main phase for both sintering temperatures (not shown). Significant differences that could suggest disparities on the

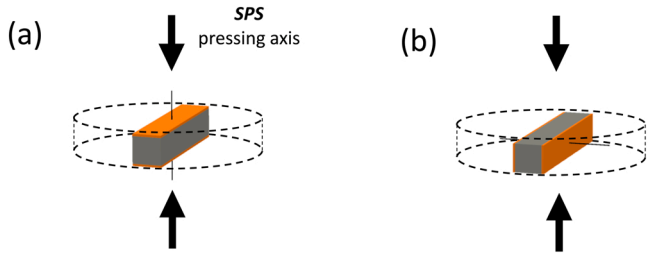

Fig. 1. Diagrams of the two electrode configurations used to obtain the electrical conductivity along the directions: (a) parallel (defined by subscript //) and (b) perpendicular (superscript ⊥) to the SPS pressing axis.

reduction rate were not observed on the diffraction patterns of the composites with different GBN content, or sintered at different temperature. The presence of a reduced state of the tetragonal phase in the composites is a consequence of sintering under a highly reducing atmosphere, as a result of the graphite mold containing the powders and the absence of oxygen (sintering under vacuum), and has been reported in previous works [9,17]. The same phenomenon is usually observed on the monolithic ceramic (results not included in this work), which shows a marked black color, consequence of the reduction, after SPS densification.

The GBN distributions throughout the ceramic matrix, assessed on the polished cross-section surfaces of the composites by BSE-SEM, are presented in Fig. 2 for the composites sintered at 1250 °C. As a consequence of the average atomic number difference between the two phases of the composite, the micrographs show a light phase corresponding to the 3YTZP matrix and a dark phase corresponding to the GBN. Significant differences are observed between the c.s. microstructures of the e-GNP and the FLG composites, as previously reported for composites with e-GNP and FLG contents up to 5 vol% [19]. While the former present an isotropic microstructure with the e-GNP oriented surrounding small zirconia zones, in the latter, a preferential FLG alignment is clearly observed, with the *ab*-plane disposed perpendicular to the direction of the applied pressure during sintering. No effect of the sintering temperature is detected on the GBN distribution within the matrix. In the composites with 10 and 20 FLG vol%, some neat ceramic areas with oval shape and presenting certain anisotropy can be observed. This behavior, not observed for the e-GNP composites, evidences that for high GBN contents the FLG did not mix with the 3YTZP ceramic powder as homogeneously as the planetary milled e-GNP. The anisotropy of the neat ceramic areas would be a consequence of the applied uniaxial pressure during sintering.

The effects of the powder processing routine as well as the sintering temperature on the structure of the two GBN incorporated to the composites have been analyzed by Raman spectroscopy. The Raman spectra of the e-GNP and FLG composites sintered at 1250 °C are presented in Fig. 3. The spectra acquired on the composites sintered at 1300 °C can be found in the Fig. S1 in the Supplementary Section. The spectra for all the e-GNP and FLG composites present the characteristic peaks of the graphitic structures: D, G and 2D peaks, centered at ~1350, ~1580 and ~2700 cm^{-1}, respectively. The preservation of the two-dimensional graphene-based nanostructures in the composites after the powder processing and sintering is confirmed by the presence of these bands. The processing routine by means of high-energy planetary ball milling introduces the most remarkable modifications in the GBN structure (Fig. 3(a)), since a significant change in the Raman spectra of the e-GNP composites is observed, with a drastic increase in the I_D/I_G ratio. After the powder processing and sintering, the Raman spectra for the e-GNP composites highly resemble the spectra acquired for the FLG composites, which points to a multilayer graphene structure of the e-GNP. In a previous work [18], devoted to the analysis of composites with e-GNP contents up to 5 vol%, a detailed study by means of integrated areas of the defect-related peaks –D, D'' (~1500–1550 cm^{-1}) and D′ (~1610–1620 cm^{-1})- of the spectra of the planetary ball milled powders and the sintered composites was carried out. Drastic increases in the I_D/I_G, $I_{D''}/I_G$ and $I_{D'}/I_G$ ratios were observed for 1 and 5 vol% e-GNP composite powders after high energy milling. The D and D′ bands are attributed to defects related to graphene layer edges and surface graphene layers, respectively [18,21]. Thus, the authors of the study [18] concluded that the planetary milling provoked the exfoliation and the lateral size reduction of the as-received GNP. It was not possible to discard the promotion of structural defects in the GNP during milling, as a decrease of the I_{2D}/I_G ratio was also observed. On the other hand, the study also revealed that a recovery of the structural damage that was induced during milling of the powders was produced during the sintering process, as decreases on the I_D/I_G, $I_{D''}/I_G$ and $I_{D'}/I_G$ ratios, together with an increase of the I_{2D}/I_G ratio, were observed. Besides, the 2D band could be fitted to three Lorentzian functions which, according to previous authors [21], indicated that the e-GNP filler presented a number of layers lower than 10 [18,21]. Regarding the FLG composites, the effects of the processing and sintering on the Raman spectra are not

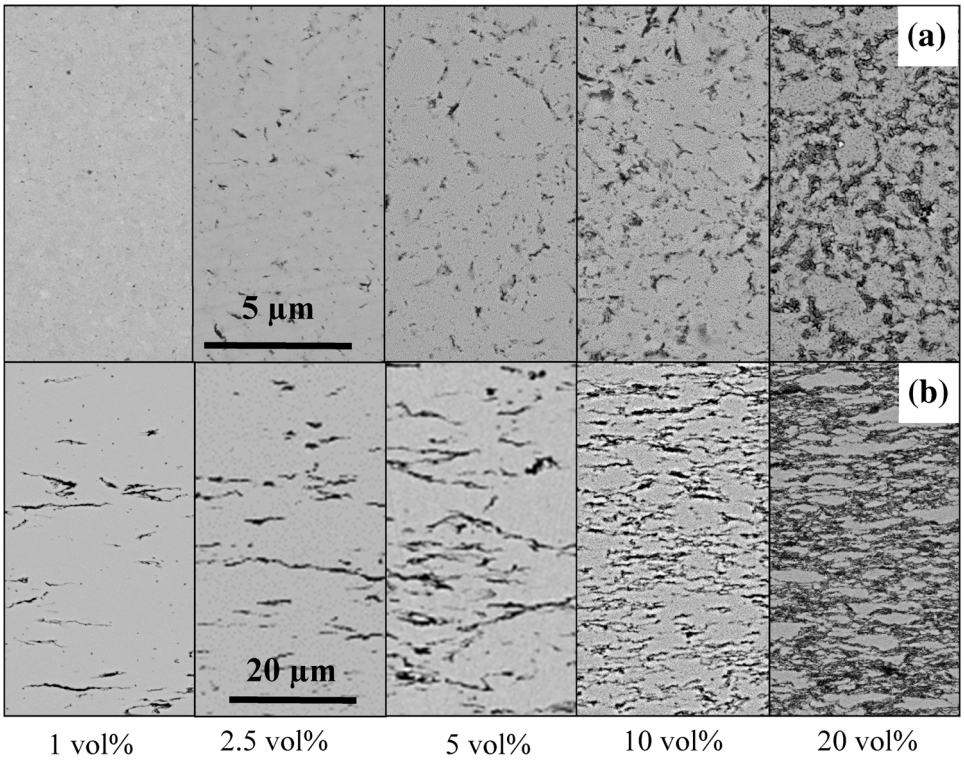

Fig. 2. BSE-SEM images from the c.s. surfaces of the composites sintered at 1250 °C (a) e-GNP composites, and (b) FLG composites.

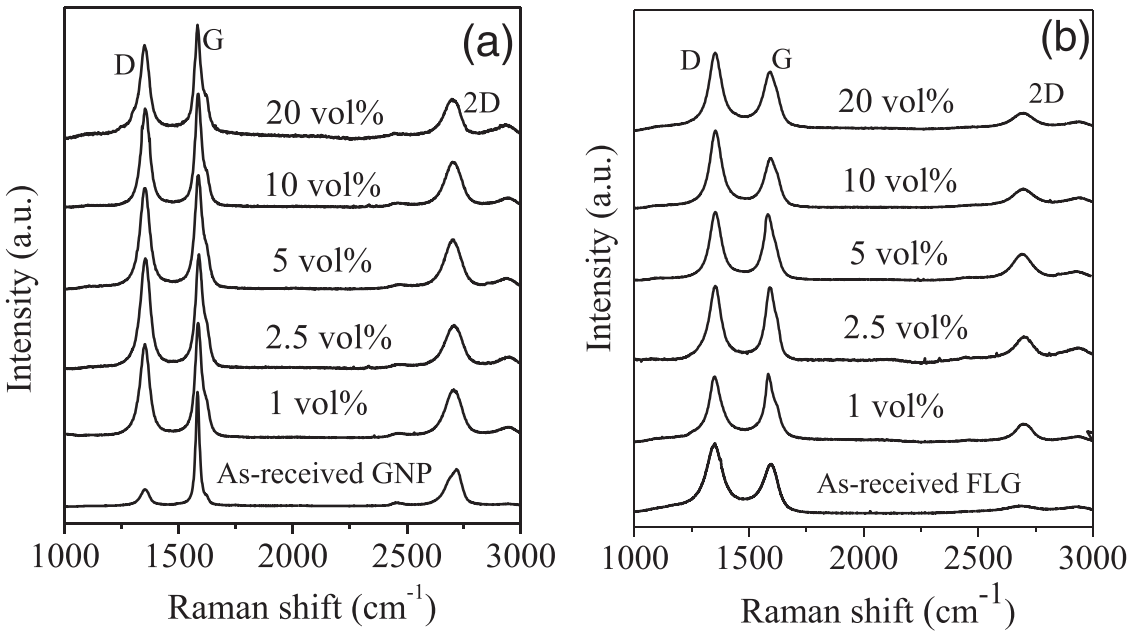

Fig. 3. Raman spectra of the composites sintered at 1250 °C: (a) e-GNP composites, (b) FLG composites. The spectra of the as-received GBN are included in order to stablish a comparison.

so remarkable visually (Fig. 3(b)). However, a restoration of the graphene structure consisting of a lower number of defects, a higher crystallinity and a lower amount of amorphous carbon in the FLG after sintering has been reported for contents up to 5 vol% [20]. The reduction on the number of defects and the amount of amorphous carbon present in the FLG during the thermal treatment was revealed by the remarkable decrease of I_D/I_G, $I_{D'}/I_G$ and $I_{D'}/I_G$, and the significant increase of I_{2D}/I_G observed in the sintered composites when comparing with the data for the as-received FLG [20]. In relation to the effect of the sintering temperature, optimized crystallinities were reported for composites with 1 and 5 vol% e-GNP [18,19] and 2.5 and 5 vol% FLG [20] when sintering at 1300 °C in comparison with the composites sintered at 1250 °C.

In the present work, the Raman study has been extended to composites with higher e-GNP and FLG contents, and very similar Raman spectra have been obtained in the whole range of contents, so it can be concluded that the effects of the powder processing and sintering are very similar to the ones already described for the composites with lower GBN contents.

Fig. 4 presents the relative densities obtained for the studied composites (data can be also found in Tables 1 and 2). All the e-GNP composites present nearly full densification, with a very slight decrease in density for the composites with 10 and 20 vol% (> 97% RD) in comparison with the composites with lower e-GNP content. In the case of the FLG composites, the decrease in density is more pronounced. It starts for lower FLG contents, and relative densities as low as 94% are obtained for the highest vol%. A significant enhancement in relative density is not observed when increasing the sintering temperature to 1300 °C (Tables 1 and 2, Fig. 4).

Since no porosity is observed along the ceramic matrix, the decrease of density in the FLG composites must be caused by the FLG. Fig. 5 shows, as an example, a high-magnification BSE-SEM image of the 10 vol% FLG composite sintered at 1300 °C where microcavities can be observed between the graphene sheets themselves and between the FLG and the ceramic matrix interfaces (marked with arrows). These microcavities were not observed in any of the e-GNP composites. This effect could be a consequence of the morphology of the FLG, with thin and wavy layers that crumple and form ripples, allowing the formation of microcavities in some parts of the FLG-ceramic interface. However, it is not possible to discard that the decrease of density in the FLG composites could be due to agglomerates present in the FLG.

3.2. Electrical conductivity

For both types of composites, an increasing trend is observed for the electrical conductivity when augmenting the GBN content, as expected (Fig. 6). This is attributed to the increase of the number of interconnections between the GBN, which enhances the electrical percolation. The electrical performance of the two types of composites is significantly different, according to the remarkable microstructural differences between them, in the whole range of GBN content. The FLG composites present a highly anisotropic conductivity with the conductivity along the direction perpendicular to the SPS pressing axis -$\sigma_\perp$- significantly higher than the one along the parallel direction -$\sigma_{//}$-. It is worth noticing that the anisotropy factor for these composites is between 10 and 20 (Table 1), very similar to the reported one for GNP/Si_3N_4 composites [22], but much higher than values previously reported for GBN/3YTZP composites [10,23]. On the other hand, the e-GNP composites are almost electrically isotropic (anisotropy factor between 1 and 2, Table 2). Çelik et al. [12] reported an electrical conductivity exhibiting just a slight anisotropy for Al_2O_3 composites with graphene platelets (GPL) even though a preferential orientation of the GPL throughout the matrix was detected by SEM. The lower electrical anisotropy than expected was attributed to the presence of misaligned/rotated GPL with respect to the alignment plane. More recently, Baskut [24] and López-Pernía et al. [17] reported that the anisotropic effect on the electrical conductivity of GPL/SiC and GNP/3YTZP composites, respectively, decreased with the reduction in the platelet size of the GPL, since this reduction led to a decrease in their orientation degree within the matrix microstructure. In the e-GNP composites studied here, it is clear that the presence of just a slight anisotropy is a consequence of the reduced e-GNP size after high-energy planetary milling, which allows the isotropic distribution of the small-size platelets in the matrix.

The highest values of $\sigma_\perp$ in this study have been obtained in the FLG composites (Table 1). The achieved conductivities present values similar to the reported ones for Si_3N_4 [22], SiC [25] or B_4C [26] composites with similar GBN contents.

Together with the high conductivity values achieved for the highest

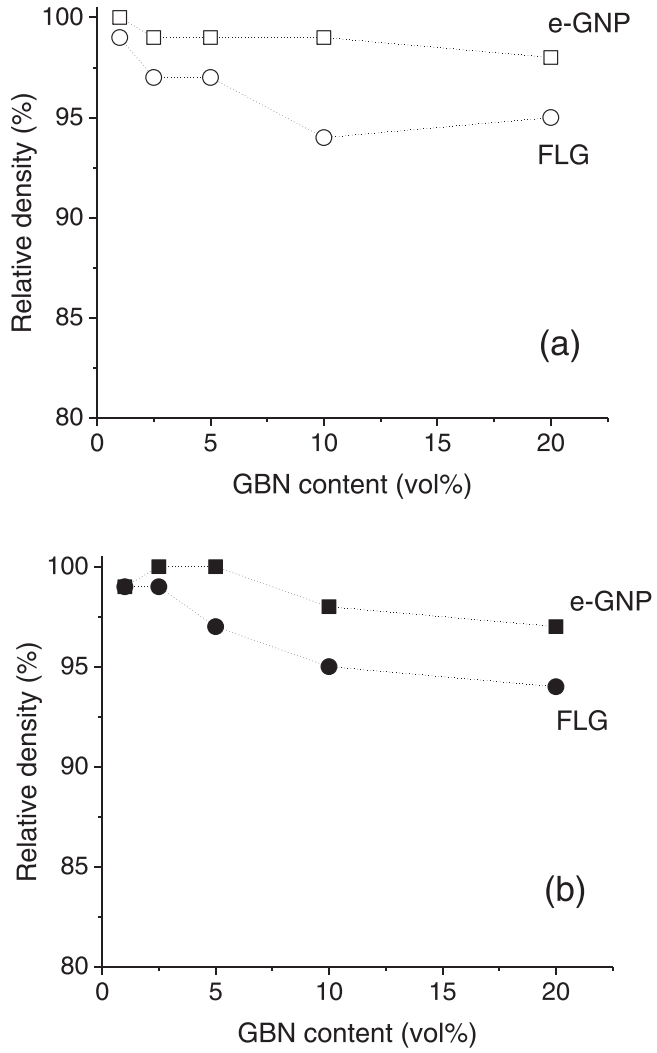

Fig. 4. Relative density of the composites sintered at (a) 1250 and (b) 1300 °C.

Table 1
Relative density, electrical conductivity and anisotropy factor for the FLG composites.

FLG vol%	Sintering Temperature (°C)	Relative density (%)	$\sigma_{\perp}$ (S/m)	$\sigma_{//}$ (S/m)	$\sigma_{\perp}/\sigma_{//}$
1	1250	99	Not conductive		
2.5		97	Not conductive*		
5		97	421*	20.9*	20.1
10		94	765	82	9.3
20		95	3220	211	15.3
1	1300	99	0.07	Not conductive	
2.5		99	49.20*	3.06*	16.1
5		97	678*	74*	9.2
10		95	608	41	14.8
20		94	4100	297	13.8

* From Ref [20]

FLG contents, a noteworthy advantage of the FLG composites with respect to the e-GNP composites is that high conductivities are also attained for lower FLG vol%. With 5 vol% FLG, conductivities in the same order of magnitude as the ones for 10 vol% FLG are reached (Table 1). It is remarkable that for 5 vol% FLG, even the $\sigma_{//}$ values are higher that the $\sigma_{\perp}$ achieved in the composite with the same e-GNP content. The obtained $\sigma_{\perp}$ would allow effective EDM according to Hanzel et al. [27], who pointed out a minimum value of ~500 S/m for

Table 2
Relative density, electrical conductivity and anisotropy factor for the e-GNP composites.

e-GNP vol%	Sintering Temperature (°C)	Relative density (%)	$\sigma_{\perp}$ (S/m)	$\sigma_{//}$ (S/m)	$\sigma_{\perp}/\sigma_{//}$
1	1250	100	Not conductive		
2.5		99	Not conductive		
5		99	6.49	3.08	2.1
10		99	471**	406**	1.2
20		98	2800	1670	1.7
1	1300	99	Not conductive		
2.5		100	0.03	Not conductive*	
5		100	18.12	12.30*	1.5
10		98	655	379	1.7
20		97	3180	1871	1.7

* From Ref [19]
** From Ref [17]

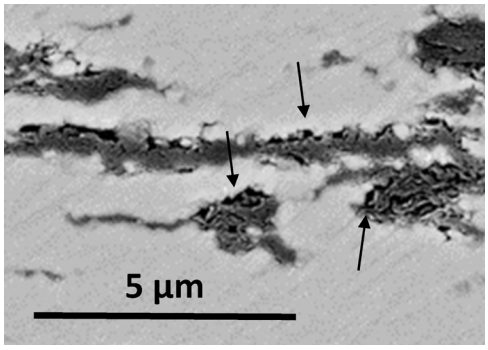

Fig. 5. BSE-SEM image from the c.s. surface of the 10 vol% FLG composite sintered at 1300 °C showing microcavities between the graphene sheets and between the FLG and the ceramic (marked with arrows).

the machined materials. Moreover, the conductivities for 5 vol% FLG are also higher than the reported ones by Chen et al. [4] (~100 S/m) for SiC with 3 wt% GNP composites with extremely high values of electromagnetic interference (EMI) shielding effectiveness.

A significant conductivity is also achieved in the composite with 2.5 vol% FLG sintered at 1300 °C, with $\sigma_{\perp}$ and $\sigma_{//}$ in the same order than the values reported by Flaureau et al. [10] for a 3YTZP/FLG composite with similar FLG content but sintered from powders prepared by CVD of carbon onto the zirconia powder. In their study, the composites presented a continuous FLG film over long distances as opposed to the discrete micron-sized FLG platelets of the present study. However, the anisotropy factor reported by these authors [10] is lower than the one presented here due to the fact that $\sigma_{//}$ in their study is 10 times higher than the reported in the present study. This is probably due to the fact that in the mentioned work FLG are uniformly wrapping the 3YTZP.

Regarding the e-GNP composites, the homogeneous e-GNP distribution throughout the ceramic matrix (Fig. 2(a)), has resulted in an excellent electrical performance for the composites with 10 and 20 e-GNP vol%. On the one hand, the values of $\sigma_{\perp}$ are almost as high as the achieved ones for the FLG composites. On the other hand, the values of $\sigma_{//}$ are significantly higher for the e-GNP composites than for the FLG composites. Both $\sigma_{\perp}$ and $\sigma_{//}$ are close to 500 S/m for the composite with 10 vol% e-GNP, which, as previously mentioned, would allow the effective EDM industrial process in both directions of the sample. This fact turns this composite into a very attractive material, as it would allow the miniaturization of micro-parts with complex geometries, by using cost-effective GNP as starting GBN.

The described differences between the FLG and e-GNP composites can be explained by taking into account how the conduction takes place in graphene containing ceramic composites, and the different factors

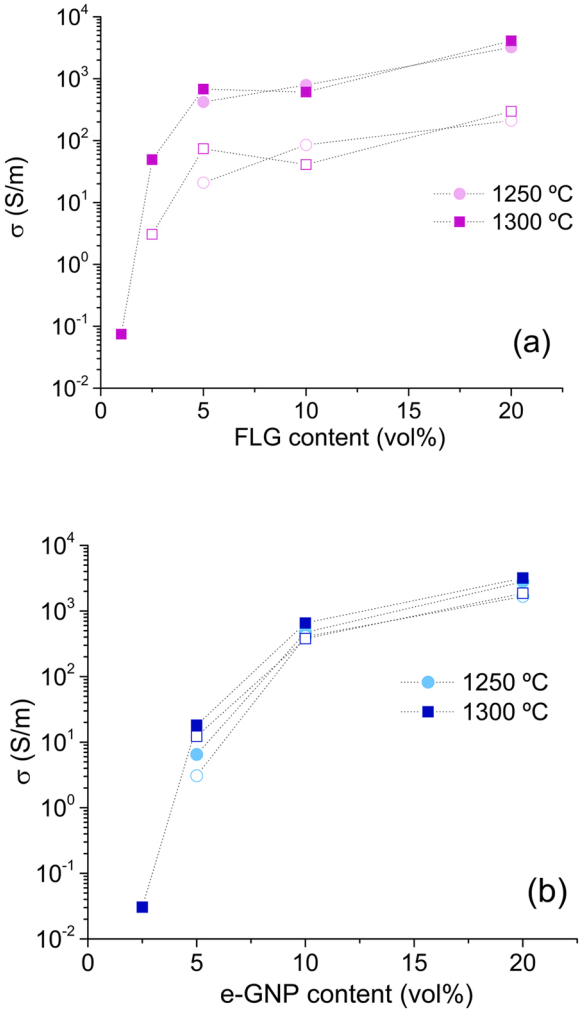

Fig. 6. Electrical conductivity as a function of the GBN content of the composites sintered at 1250 and 1300 °C, (a) FLG and (b) e-GNP. Full symbols: $\sigma_{\perp}$, open symbols: $\sigma_{//}$.

that have an influence on the process. Electrical conductivity is generated by the transport of electrons through the GBN and by the transfer of electrons from one GBN to another in the non-conductive ceramic matrix. Thus, the intrinsic conductivity of the GBN together with the resistance generated by the transfer of electrons between adjacent GBN should be considered.

For composites with high GBN contents, electron conduction occurs through direct contact between the graphene nanostructures. It has been reported that the contact resistance is highly dependent on the number of graphene layers in the GBN [28], resulting in high resistance values at the junctions of thick GBN, while low resistances occur between thin/individual GBN. Furthermore, a significant dependence of the intrinsic electrical conductivity of multilayer graphene on the number of graphene layers has been also reported [28,29]. Numerical simulations performed by Fang et al. [29] on monolayer graphene, FLG (2–9 layers) and graphene nanosheets (>10 layers; ~3–100 nm thickness) revealed that the decrease in the electrical conductivity of few-/multi-layer graphene with respect to the conductivity of single layer graphene was caused by the inhibition of charge carriers movement due to three-dimensional scattering at the interlayer channels with the increasing number of graphene layers. The calculations were in agreement with the experimental results of Nirmalraj et al. [28], who reported higher conductivity of the FLG than that of graphene nanosheets by using conductance imaging atomic force microscopy. As previously mentioned in Section §3.1, the Raman analysis performed in a former study on 1 and 5 vol% e-GNP composites [18] revealed that the decrease in the number of structural defects during sintering had an effect on the intensity (remarkable increase of the I_{2D}/I_G ratio) and shape of the second-order spectra. The fitting of the 2D band to three Lorentzian functions evidenced that the e-GNP filler presents a number of graphene layers lower than 10 after exfoliation during the high-energy planetary milling of the powders [18,21]. However, it is not possible by means of this type of fitting to assure that the exfoliation has turned the as-received GNP into few layer graphene. Thus, it is likely that the e-GNP filler exhibits a higher number of graphene layers that the few layer graphene (3–5 layers). In consequence, the FLG network would present a higher electrical conductivity as a consequence of the higher intrinsic conductivity of the FLG and the lower contact resistance between them. This explains the fact that the composites with 10 and 20 vol% FLG show a slightly higher conductivity than the e-GNP composites, despite the excellent e-GNP distribution thorough the matrix (as an example, $\sigma_{\perp} =$ 3220 and 2800 S/m for the composites with 20 vol% FLG and e-GNP sintered at 1250 °C, respectively, Tables 1 and 2). Similar results have been reported by Baskut and Turan [30] for GNP/SiAlON composites. In their study, GNP with different lateral dimension and thickness were added to the matrix, and despite close lateral dimension values, the SiAlON containing the thicker GNP had the lowest electrical conductivity.

Moreover, the higher intrinsic conductivity in the *ab*-plane and lower contact resistance of the FLG, together with their preferential alignment, are responsible of the high electrical anisotropy of the FLG composites, with $\sigma_{\perp}$ remarkably higher than $\sigma_{//}$. The transport of electrons through some FLG that could be disposed in a perpendicular way with respect to most of the FLG, that is, with their *ab*-plane in the direction parallel to the SPS pressing axis, would be the origin of the $\sigma_{//}$, as previously reported [23].

For low GBN contents, when the neighboring GBN are not in physical contact in the network throughout the matrix, the tunneling effect is the main mechanism by which the electrons are transferred between the graphene nanostructures through the small isolating barriers created by the non-conductive matrix. The aspect ratio of the GBN has been pointed out as one of the parameters strongly controlling the tunneling resistance [30–32], with decreasing resistance for increasing aspect ratios. The probability of interconnection between the nanostructures is highly promoted as the GBN lateral size increases, and the electron tunneling effect raises [32]. In the present work, the difference in the aspect ratio of the two studied GBN is very noteworthy, with a much higher length/thickness ratio in the FLG, which could result in an enhanced electron tunneling effect in the FLG composites. This could be one of the effects responsible for the significantly higher conductivities obtained in the composites with low FLG vol%.

An effect of the GBN aspect ratio on the percolation threshold of graphene composites has been also reported [30,32]. In a recent study on GNP/SiAlON composites [30], the lowest percolation limits were achieved with the thinnest GNP with largest dimension and aspect ratio among the used GNP. Percolation threshold between 1.48 and 1.98 vol% and between 0.24 and 0.74 vol% have been recently reported for FLG/3YTZP [10] and FLG/Al_2O_3 [33] composites, which presented a continuous FLG film over long distances, that is, an extremely high aspect ratio. In our study, differences in the percolation limit are only observed in the composites sintered at 1300 °C, despite the significant differences in aspect ratios between FLG and e-GNP. This is because, along with the aspect ratio, there is also another effect that has a high influence on percolation by influencing the intrinsic conductivity: the presence of defects in the graphene structure. The transport properties of graphene with point defects essentially depend on the imperfection of the hexagonal carbon atom network and the scattering of carriers by localized states [34]. Defects as vacancies or heptagon-pentagon structures act as local scattering centers of carriers and reduce electrical conductance of graphene [34]. An increase of the resistance has been also reported for multilayer graphene after inducing surface defects and

nanoholes by irradiation with Ar plasma [35]. The presence of amorphous carbon in the FLG structure has been also pointed out as responsible for hampering the electrical conductivity of FLG composites [20].

When sintering at high temperature, a restoration of the graphene structure is provoked, achieving a reduction in the number of defects and the amount of amorphous carbon, as previously described in Section §3.1. For the highest sintering temperature (1300 °C) the structure restoration is more pronounced, which results in an enhanced electrical conductivity both in $\sigma_{//}$ and $\sigma_{\perp}$, for each GBN vol% in both types of composites (Tables 1 and 2), and a decrease of the percolation threshold. The effect is more remarkable for the FLG composites, as a consequence of the higher aspect ratio of FLG, achieving a percolation limit below 2.5 vol% FLG, similar to the reported one by Flaureau et al. [10] for 3YTZP composites with extremely high aspect ratio FLG.

4. Conclusions

Orthotropic and isotropic 3YTZP composites have been obtained by incorporating few layer graphene (FLG) or exfoliated graphene nanoplatelets (e-GNP), respectively, as fillers. In the latter case, the e-GNP present small lateral size and are randomly oriented in the matrix. In the former case, the FLG present high aspect ratio, low thickness and are preferentially oriented perpendicular to the SPS pressing direction.

The isotropic e-GNP composites with high contents present an excellent electrical conductivity, with $\sigma_{//}$ values higher than the FLG composites, as a consequence of the misoriented e-GNP distribution throughout the ceramic matrix. However, the low aspect ratio and high thickness of the e-GNP hinder the conductivity at low e-GNP contents, due to the higher tunneling resistance and lower intrinsic conductivity.

Optimum electrical performance was achieved in the highly anisotropic FLG composites, with high electrical conductivity for only 5 vol%, percolation threshold below 2.5 vol% and outstanding electrical conductivity for high contents ($\sigma_{\perp} \sim 4000$ S/m for 20 vol% FLG sintered at 1300 °C). As a result of the high aspect ratio, low thickness and decreased number of defects of FLG after sintering at the highest temperature, the tunneling and contact resistance were decreased, and the intrinsic conductivity was enhanced in these composites. Tailoring of the electrical performance of these type of materials will allow their use on demand depending on the specific requirements of different engineering applications.

Declaration of Competing Interest

The authors declare that they have no known competing financial interests or personal relationships that could have appeared to influence the work reported in this paper.

Acknowledgements

This research was supported by project PGC2018–101377-B-100 funded by MCIN/AEI/ 10.13039/501100011033 (Ministerio de Ciencia e Innovación, Spanish Government, Agencia Estatal de Investigación) and ERDF (European Regional Development Funding) "A way of making Europe", by the European Union and by project P20_01024 (Junta de Andalucía/FEDER, UE 2014–2020). C. López-Pernía acknowledges the financial support of MINECO (Ministerio de Economía y Competitividad, Spanish Government) through the FPI contract ref: BES-2016- 078711. C. Muñoz-Ferreiro acknowledges the financial support of a VI PPIT-US (Plan Propio Universidad de Sevilla, Spain) fellowship through the contract USE-18740-H.

Appendix A. Supporting information

Supplementary data associated with this article can be found in the online version at doi:10.1016/j.jeurceramsoc.2022.11.068.

References

[1] C. Ramírez, M. Belmonte, P. Miranzo, M.I. Osendi, Applications of ceramic/graphene composites and hybrids, Mater. (Basel) 14 (2021) 2071–2133, https://doi.org/10.3390/ma14082071.
[2] P. Miranzo, M. Belmonte, M.I. Osendi, From bulk to cellular structures: a review on ceramic/graphene filler composites, J. Eur. Ceram. Soc. 37 (2017) 3649–3672, https://doi.org/10.1016/j.jeurceramsoc.2017.03.016.
[3] A. Nieto, A. Bisht, D. Lahiri, C. Zhang, A. Agarwal, Graphene reinforced metal and ceramic matrix composites: a review, Int. Mater. Rev. 62 (2017) 241–302, https://doi.org/10.1080/09506608.2016.1219481.
[4] C. Chen, Y. Tan, X. Han, H. Luo, S. Zeng, S. Peng, H. Zhang, Enhanced electromagnetic interference shielding properties of silicon carbide composites with aligned graphene nanoplatelets, J. Eur. Ceram. Soc. 38 (2018) 5615–5619, https://doi.org/10.1016/j.jeurceramsoc.2018.07.050.
[5] A. Nieto, J.M. Zhao, Y.-H. Han, K.H. Hwang, J.M. Schoenung, Microscale tribological behavior and in vitro biocompatibility of graphene nanoplatelet reinforced alumina, J. Mech. Behav. Biomed. Mater. 61 (2016) 122–134, https://doi.org/10.1016/j.jmbbm.2016.01.020.
[6] O. Tapasztó, L. Tapasztó, H. Lemmel, V. Puchy, J. Dusza, C. Balázsi, K. Balázsi, High orientation degree of graphene nanoplatelets in silicon nitride composites prepared by spark plasma sintering, Ceram. Int. 42 (2016) 1002–1006, https://doi.org/10.1016/j.ceramint.2015.09.009.
[7] O. Hanzel, R. Sedlák, J. Sedláček, V. Bizovská, R. Bystrický, V. Girman, A. Kovalčíková, J. Dusza, P. Šajgalík, Anisotropy of functional properties of SiC composites with GNPs, GO and in-situ formed graphene, J. Eur. Ceram. Soc. 37 (2017) 3731–3739, https://doi.org/10.1016/j.jeurceramsoc.2017.03.060.
[8] S. Baskut, A. Cinar, A.T. Seyhan, S. Turan, Tailoring the properties of spark plasma sintered SiAlON containing graphene nanoplatelets by using different exfoliation and size reduction techniques: anisotropic electrical properties, J. Eur. Ceram. Soc. 38 (2018) 3787–3792, https://doi.org/10.1016/j.jeurceramsoc.2018.04.066.
[9] C. Muñoz-Ferreiro, A. Morales-Rodríguez, T.C. Rojas, E. Jiménez-Piqué, C. López-Pernía, R. Poyato, A. Gallardo-López, Microstructure, interfaces and properties of 3YTZP ceramic composites with 10 and 20 vol% different graphene-based nanostructures as fillers, J. Alloy. Compd. 777 (2019) 213–224, https://doi.org/10.1016/j.jallcom.2018.10.336.
[10] A. Flaureau, A. Weibel, G. Chevallier, J. Esvan, C. Laurent, C. Estournès, Few-layered-graphene/zirconia composites: Single-step powder synthesis, spark plasma sintering, microstructure and properties, J. Eur. Ceram. Soc. 42 (2022) 2349–2361, https://doi.org/10.1016/j.jeurceramsoc.2022.01.006.
[11] N. Obradović, F. Kern, Properties of 3Y-TZP zirconia ceramics with graphene addition obtained by spark plasma sintering, Ceram. Int. 44 (2018) 16931–16936, https://doi.org/10.1016/j.ceramint.2018.06.133.
[12] Y. Çelik, A. Çelik, E. Flahaut, E. Suvaci, Anisotropic mechanical and functional properties of graphene-based alumina matrix nanocomposites, J. Eur. Ceram. Soc. 36 (2016) 2075–2086, https://doi.org/10.1016/j.jeurceramsoc.2016.02.032.
[13] Q. Wang, C. Ramírez, C.S. Watts, O. Borrero-López, A.L. Ortiz, B.W. Sheldon, N. P. Padture, Fracture, fatigue, and sliding-wear behavior of nanocomposites of alumina and reduced graphene-oxide, Acta Mater. 186 (2020) 29–39, https://doi.org/10.1016/j.actamat.2019.12.035.
[14] C. Ojalvo, R. Moreno, F. Guiberteau, A.L. Ortiz, Processing of orthotropic and isotropic superhard B_4C composites reinforced with reduced graphene oxide, J. Eur. Ceram. Soc. 40 (2020) 3406–3413, https://doi.org/10.1016/j.jeurceramsoc.2020.02.027.
[15] C. López-Pernía, Á. Gallardo-López, A. Morales-Rodríguez, R. Poyato, Graphene nanoplatelets for electrically conductive 3YTZP composites densified by pressureless sintering, J. Eur. Ceram. Soc. 39 (2019) 4435–4439, https://doi.org/10.1016/j.jeurceramsoc.2019.05.067.
[16] C. Ojalvo, R. Moreno, F. Guiberteau, A.L. Ortiz, Pressureless ultrafast sintering of near-net-shaped superhard isotropic B_4C/rGO composites with Ti-Al additives, J. Eur. Ceram. Soc. 40 (2020) 4354–4360, https://doi.org/10.1016/j.jeurceramsoc.2020.05.033.
[17] C. López-Pernía, C. Muñoz-Ferreiro, C. González-Orellana, A. Morales-Rodríguez, Á. Gallardo-López, R. Poyato, Optimizing the homogenization technique for graphene nanoplatelet/yttria tetragonal zirconia composites: influence on the microstructure and the electrical conductivity, J. Alloy. Compd. 767 (2018) 994–1002, https://doi.org/10.1016/j.jallcom.2018.07.199.
[18] Á. Gallardo-López, J. Castillo-Seoane, C. Muñoz-Ferreiro, C. López-Pernía, A. Morales-Rodríguez, R. Poyato, Flexure strength and fracture propagation in zirconia ceramic composites with exfoliated graphene nanoplatelets, Ceramics 3 (2020) 78–91, https://doi.org/10.3390/ceramics3010009.
[19] A. Morales-Rodríguez, C. González-Orellana, A.A. Pérez-García, C. López-Pernía, C. Muñoz-Ferreiro, R. Poyato, Á. Gallardo-López, Ageing-resistant zirconia/graphene-based nanostructures composites for use as biomaterials, J. Eur. Ceram. Soc. 42 (2022) 1784–1795, https://doi.org/10.1016/j.jeurceramsoc.2021.11.060.
[20] C. Muñoz-Ferreiro, C. López-Pernía, Á. Gallardo-López, R. Poyato, Unravelling the optimization of few-layer graphene crystallinity and electrical conductivity in ceramic composites by Raman spectroscopy, J. Eur. Ceram. Soc. 41 (2021) 290–298, https://doi.org/10.1016/j.jeurceramsoc.2021.09.025.
[21] A.C. Ferrari, D.M. Basko, Raman spectroscopy as a versatile tool for studying the properties of graphene, Nat. Nanotechnol. 8 (2013) 235–246, https://doi.org/10.1038/nnano.2013.46.
[22] C. Ramirez, F.M. Figueiredo, P. Miranzo, P. Poza, M.I. Osendi, M. Isabel Osendi, Graphene nanoplatelet/silicon nitride composites with high electrical conductivity, Carbon N.Y. 50 (2012) 3607–3615, https://doi.org/10.1016/j.carbon.2012.03.031.

[23] R. Poyato, J. Osuna, A. Morales-Rodríguez, Á. Gallardo-López, Electrical conduction mechanisms in graphene nanoplatelet/yttria tetragonal zirconia composites, Ceram. Int. 44 (2018) 14610–14616, https://doi.org/10.1016/j.ceramint.2018.05.082.
[24] S. Baskut, The effects of thermal conductivity and anisotropy on the electro discharge machinability of ceramics containing graphene platelets, Mater. Chem. Phys. 283 (2022), 126054, https://doi.org/10.1016/j.matchemphys.2022.126054.
[25] B. Román-Manso, E. Domingues, F.M. Figueiredo, M. Belmonte, P. Miranzo, Enhanced electrical conductivity of silicon carbide ceramics by addition of graphene nanoplatelets, J. Eur. Ceram. Soc. 35 (2015) 2723–2731, https://doi.org/10.1016/j.jeurceramsoc.2015.03.044.
[26] A. Wang, L. Hu, Q. He, C. Liu, T. Tian, Z. Zhang, C. Yi, F. Zhang, W. Wang, H. Wang, Z. Fu, Electrical discharge machining of boron carbide-graphene nanoplatelets composites, J. Eur. Ceram. Soc. 42 (2022) 850–859, https://doi.org/10.1016/j.jeurceramsoc.2021.11.018.
[27] O. Hanzel, M.A. Singh, D. Marla, R. Sedlák, P. Šajgalík, Wire electrical discharge machinable SiC with GNPs and GO as the electrically conducting filler, J. Eur. Ceram. Soc. 39 (2019) 2626–2633, https://doi.org/10.1016/j.jeurceramsoc.2019.03.012.
[28] P.N. Nirmalraj, T. Lutz, S. Kumar, G.S. Duesberg, J.J. Boland, Nanoscale mapping of electrical resistivity and connectivity in graphene strips and networks, Nano Lett. 11 (2011) 16–22, https://doi.org/10.1021/nl101469d.
[29] X.Y. Fang, X.X. Yu, H.M. Zheng, H.B. Jin, L. Wang, M.S. Cao, Temperature- and thickness-dependent electrical conductivity of few-layer graphene and graphene nanosheets, Phys. Lett. Sect. A Gen. Solid State Phys. 379 (2015) 2245–2251, https://doi.org/10.1016/j.physleta.2015.06.063.
[30] S. Baskut, S. Turan, The effect of different GNPs addition on the electrical conductivities and percolation thresholds of the SiAlON matrix composites, J. Eur. Ceram. Soc. 40 (2020) 1159–1167, https://doi.org/10.1016/j.jeurceramsoc.2019.11.057.
[31] S. Baskut, Effects of adding GPLs dispersed at different sonication times on the thermal and electrical conductivities of spark plasma sintered silicon carbide, Mater. Chem. Phys. 287 (2022), 126230, https://doi.org/10.1016/j.matchemphys.2022.126230.
[32] J. Payandehpeyman, M. Mazaheri, M. Khamehchi, Prediction of electrical conductivity of polymer-graphene nanocomposites by developing an analytical model considering interphase, tunneling and geometry effects, Compos. Commun. 21 (2020), 100364, https://doi.org/10.1016/j.coco.2020.100364.
[33] A. Weibel, A. Flaureau, A. Pham, G. Chevallier, J. Esvan, C. Estournès, C. Laurent, One-step synthesis of few-layered-graphene/alumina powders for strong and tough composites with high electrical conductivity, J. Eur. Ceram. Soc. 40 (2020) 5779–5789, https://doi.org/10.1016/j.jeurceramsoc.2020.06.029.
[34] N. Liu, S. Zhou, J. Zhao, Electrical conductance of graphene with point defects, Wuli Huaxue Xuebao/ Acta Phys. - Chim. Sin. 35 (2019) 1142–1149, https://doi.org/10.3866/PKU.WHXB201810040.
[35] K. Thiyagarajan, A. Ananth, B. Saravanakumar, Y.S. Mok, S.J. Kim, Defect-induced metallic-to-semiconducting transition in multilayer graphene, RSC Adv. 5 (2015) 16821–16827, https://doi.org/10.1039/c4ra13703e.